

Formation and Characterization of 2D Closely Packed Arrays of Bare Gold Nanoparticles without Aggregation

Takashi Fujita and Kohei Shibamoto*

Cite This: *ACS Omega* 2022, 7, 44711–44719

Read Online

ACCESS |



Metrics & More

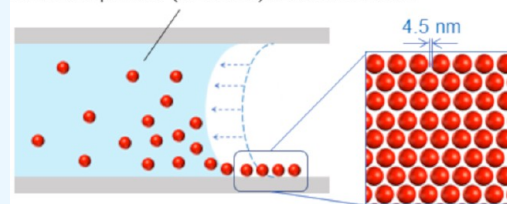


Article Recommendations



Supporting Information

ABSTRACT: Uniform 2D arrays of metal nanoparticles (NPs) have received significant attention in the field of molecular sensing using localized surface plasmon resonance. Generally, metal NPs bear organic surface-modifying molecules to prevent aggregation and form 2D metal NP arrays. However, surface-modifying molecules negatively affect molecular sensing. Previously, we developed a technique for forming a 2D bare metal NP array, denoted the sandwich (SW) technique. However, the formation mechanism of these 2D metal NP arrays remains unknown and therefore the experimental conditions of the SW technique are not optimized. Here, we observed the formation of a 2D Au NP (d : 60 nm) array using the SW technique with an optical microscope. Moderate drying conditions of the colloidal droplets sandwiched between two parallel substrates were necessary for forming 2D Au NP arrays. We then optimized the drying conditions and obtained a 2D Au NP array. This array was uniform, and the Au NPs were arranged at distances of 4.5 nm with hexagonal periodicity, without aggregation. Further, the 2D Au NP arrays exhibited excellent spot-to-spot reproducibility in surface-enhanced Raman scattering.

Gold nanoparticle (d : 60 nm) colloidal solution

The 2D array of bare gold nanoparticles has a high potential for plasmonic substrates such as SERS sensing.

INTRODUCTION

Metal nanoparticle (NP) assemblies have attracted considerable interest because of their exceptional optical properties based on localized surface plasmon resonance (LSPR), which is a collective oscillation of free electrons within the NPs.^{1,2} Under LSPR excitation, excited electrons are localized on the surfaces of metal NPs. A strong electromagnetic (EM) field is generated from the surface at a distance similar to the diameter of the metal NP. The EM field is particularly strong at an interparticle gap of several nanometers, denoted as a “hot spot”, owing to the coupling of LSPRs between adjacent NPs.³ This large EM field significantly increases the spectroscopic signals of molecules in the vicinity of metal NPs. For example, Raman scattering light of molecules is significantly enhanced in the vicinity of metal NPs by several orders of magnitude compared to normal Raman scattering light, which is called surface-enhanced Raman scattering (SERS). SERS allows the label-free identification of ultra-trace molecules. Therefore, metal NP assemblies with high-density hot spots exhibit potential as highly sensitive molecular sensors.^{4,5} However, high-density hot spots are likely to cause randomness in the strength of the EM field because the EM field strength at the hot spot is sensitive to the interparticle distance. This randomness due to the nanostructure significantly reduces the spot-to-spot reproducibility in molecular sensing.^{6,7} Therefore, the fabrication of uniform metal NP assemblies is required.

2D metal NP arrays, wherein metal NPs are densely arranged at equal interparticle distances of several nanometers, are promising candidates for generating such uniform metal NP

assemblies. Two approaches are proposed for the design of 2D metal NP arrays. A top-down approach such as electron or ion beam lithography yields precise metal NP arrays,^{8,9} but a method of generating hot spots at interparticle gaps is physically and technically challenging due to their spatial resolution. In addition, this approach generally requires large equipment and is costly. The other approach is a bottom-up approach, wherein metal NPs are assembled using a colloidal solution at liquid–liquid,^{10,11} air–liquid,^{12,13} or liquid–solid^{14,15} interfaces. In principle, this approach may form hot spots at interparticle gaps because the interaction length of interparticle repulsion between NPs in solution is of several nanometers. Moreover, it is a low-cost approach and is suitable for mass production. Hence, the bottom-up approach is promising for producing 2D metal NP arrays for use in molecular sensing, but forming a uniform 2D metal NP array remains quite challenging.

The difficulty in forming a uniform 2D metal NP array using a bottom-up approach is mainly due to the aggregation of metal NPs, which renders the interparticle distance uncontrollable. According to Derjaguin–Landau–Verwey–Overbeek (DLVO) theory, the dispersion or aggregation of particles is determined

Received: June 28, 2022

Accepted: October 28, 2022

Published: November 30, 2022



by the energy potential expressed by the sum of van der Waals attraction and electrostatic repulsion, which depend on the interparticle distance.¹⁶ Metal particles exhibit relatively strong van der Waals attractions compared to those of non-metal particles and thus easily aggregate. Relatively large metal NPs, in particular, with diameters of 50–100 nm, which exhibit relatively large SERS enhancement,^{17,18} are more likely to aggregate because they display larger van der Waals attractions than those of small metal NPs. To prevent aggregation of metal NPs, their surfaces are generally modified using organic molecules, such as alkanethiol,^{19–21} or cetyltrimethylammonium bromide.²² However, their introduction on the metal NPs causes several disadvantages and degrades the NP properties, such as shortening the lifetimes of 2D metal NP arrays, inhibiting sample molecule entry into hot spots, and hindering sample identification due to their SERS signals.^{23,24} Uniform 2D metal NP arrays without organic surface-modified molecules are desirable in molecular sensing; however, reports on bare uniform 2D metal NP arrays are limited.

To suppress the aggregation of bare metal NPs, the repulsion should dominate the van der Waals attraction until just prior to metal NP assembly. We previously suppressed the aggregation of bare Au NPs trapped at a liquid–liquid interface using the LSPR excitation of Au NPs to enhance the repulsion during the 2D Au NP array formation.²⁵ However, aggregation was not eliminated because a 3D fluctuation of the liquid–liquid interface interfered with the ordered assembly of the Au NPs. Thus, the key to forming a 2D bare metal NP array without aggregation is the assembly of metal NPs on a rigid surface as gently as possible without disturbing the attraction–repulsion balance between the metal NPs.

In addition, we developed another technique for assembling bare metal NPs at a liquid–solid interface, denoted as the “sandwich (SW) technique.”²⁶ The SW technique may yield 2D arrays of bare metal NPs with diameters of 5–200 nm by naturally drying the droplet of metal NP colloidal solution between two flat plates until complete evaporation. However, the formation mechanism of the 2D metal NP array remains unclear, and accordingly the experimental conditions of the SW technique are not optimized. Consequently, this technique exhibits low reproducibility in forming the 2D metal NP array, and the uniformity of the 2D metal NP array has not been evaluated. In this study, we initially determined the features of the formation of a 2D metal NP array by observing the formation via the SW technique using an optical microscope. Spherical Au NPs with diameters of 60 nm were used as the building blocks of the 2D metal NP array because of their excellent chemical stabilities and relatively high efficiencies of LSPR excitation. The drying conditions were then optimized. The 2D Au NP array was characterized using scanning electron microscopy (SEM) and ultraviolet–visible spectroscopy. Finally, to demonstrate the uniformity of the EM field generated on the 2D Au NP array and its potential as an optical molecular sensor, the spot-to-spot reproducibility of SERS was evaluated.

EXPERIMENTAL SECTION

Preparations of Au NP Arrays. An aqueous colloidal solution of spherical Au NPs (diameter: 60 nm; density: 2.6×10^{10} particles/mL) with a narrow size distribution was purchased from British Biocell International (Cardiff, UK). Glass slides (thickness: 1 mm) were purchased from Matsunami Glass (Bellingham, WA, USA), and Si single crystals (100 μm) were purchased from Nilaco (Tokyo, Japan). These glass slides

and Si single crystals were cleaned several times using acetone, methanol, and deionized water in an ultrasonic bath prior to use.

The colloidal solution of Au NPs (100 μL) was dropped onto a glass slide or Si single crystal. A glass slide was placed on top of the droplet, 1 mm from the bottom glass. The sandwiched droplet was placed in a thermo-hygrostat bath until the solution evaporated completely after ≤ 2 d. The substrate prepared using this technique is denoted as “SW substrate.” SW substrates were prepared under two sets of conditions: $60 \pm 10\%$ relative humidity at 298 K and $20 \pm 5\%$ relative humidity at 298 K for SW-substrates 1 and 2, respectively.

Two other substrates were prepared using oil–water trapping (OW)¹⁰ and dried droplet (DD) techniques for comparison. In the OW technique, the colloidal Au NP solution (5 mL) was transferred into a 20 mL glass vial, and toluene (5 mL) was added. After an interface formed between the toluene and the Au NP colloidal solution, methanol (5 mL) was rapidly injected into the vial, inducing the 2D trapping of the Au NPs at the interface. Then, the trapped Au NP sheet was placed on a 5×5 mm glass slide by aspirating off the solvent. The prepared OW substrates were dried in a drying cabinet at 298 K. In the DD technique, the colloidal Au NP solution (400 μL) was dropped onto a glass slide, and it was dried in a drying cabinet at 298 K.

All substrates were rinsed with deionized water to eliminate inorganic surfactants and dried further in a drying cabinet at 298 K.

Characterizations of 2D Au NP Arrays. All the substrates were observed using SEM (VE-9800, Keyence, Itasca, IL, USA) at an accelerating voltage of 20 kV. Visible–near-infrared (vis–NIR) extinction spectroscopy was performed under normal incidence conditions using a custom-built optical system connected to a spectrometer combined with an optical microscope. The focal spot diameter was confirmed using an optical microscope as $\sim 100 \mu\text{m}$.

A custom-built system was also used to conduct the Raman measurements using a 532 nm Nd:YAG laser as an excitation source. The laser power at the sample position was 5 mW, with a laser focal spot of $\sim 10 \mu\text{m}^2$. Raman spectroscopy was performed using a $-15 \text{ }^\circ\text{C}$ air-cooled spectrometer (PMA-11, Hamamatsu Photonics, Hamamatsu, Japan) that was connected to a detector. Crystal violet (CV) was used as a test molecule to perform SERS investigations. Each prepared substrate was immersed in a 10^{-5} M CV aqueous solution for 10 min to achieve saturated adsorption of CV. The substrates were then rinsed with pure water to remove any non-chemisorbed CV molecules. The Raman spectra of the adsorbed CV molecules were recorded by integrating five spectra with an exposure time of 10 s. The difference in the focus of the different substrates was calibrated using a Si band (520 cm^{-1}). The spectral signal representing CV is due to SERS light and fluorescence. The fluorescence component was removed from the raw data using the fluorescence spectrum of solid CV, and the intensity of the Raman scattered light was extracted.

RESULTS AND DISCUSSION

Formation of 2D Au NP Arrays Using the SW Technique. The formation of a 2D Au NP array using the SW technique was observed using an optical microscope. Figure 1a shows an optical microscopy image of the lateral meniscus formed by the SW technique. The meniscus exhibits a half-moon shape, which differs from those of simple droplets on a flat plate. The contact angle of the meniscus is 0° . Figure 1b shows the images of the contact line at 30 min intervals during the initial

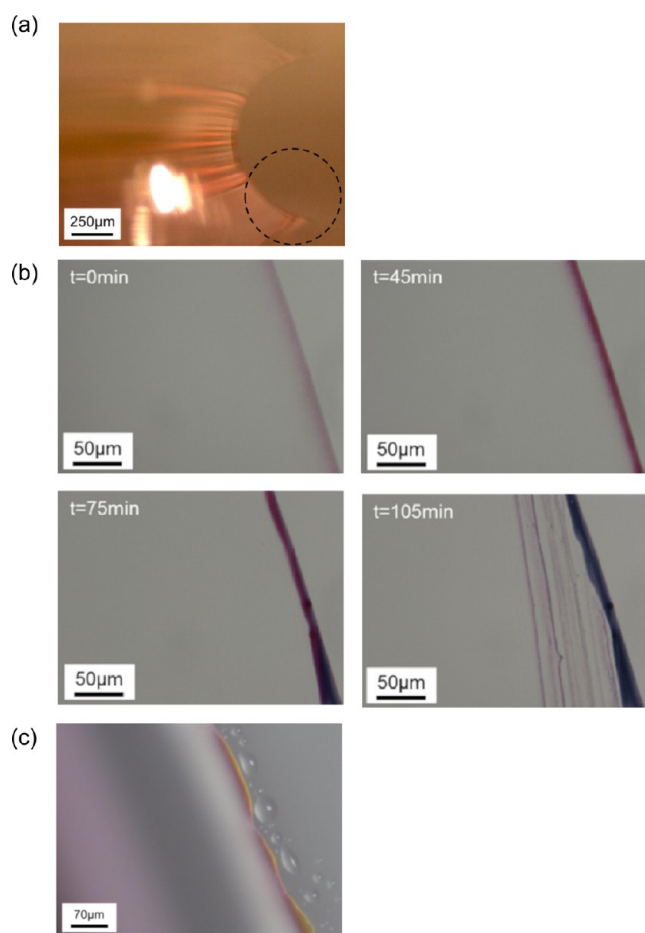


Figure 1. (a) Optical microscopy image of the lateral meniscus image formed by the SW method at 0 min from the start. Dotted circle indicates a contact line. (b) Optical microscopy image of the contact line in the initial evaporation process (0, 45, 75, and 105 min from the start). (c) Reflection microscopy image of the contact line at $t = 45$ min.

evaporation stages. At $t = 45$ min, the contact line is red due to the LSPR of the isolated Au NPs. The color of the contact line darkens with time until $t = 45$ min, with this color change corresponding to an increase in the concentration of the Au NP colloidal solution, that is, as the droplet evaporates, the Au NPs are concentrated at the edge of the contact line. From $t = 45$ to 105 min, the color of the contact line changes from red to deep purple. To observe this color change more clearly, the contact line at $t = 45$ min was observed using a reflection optical microscope, as shown in Figure 1c. A color gradation from red to gold is observed at the edge of the contact line. This gold color corresponds to an assembly of Au NPs, as confirmed by the SEM observations described below, indicating that the 2D Au NP array is formed at the edge of the contact line. At $t = 105$ min, the formation of a step-by-step structure is observed, corresponding to the structure observed using SEM (Figure 2a). This step-by-step structure indicates a gradual inward movement of the contact line because the 2D Au NP array is only formed at the edge of the contact line. Hence, the Au NP array is formed by an increase in the concentration of Au NPs at the contact line and the movement of the contact line during droplet evaporation. Therefore, the duration of the sandwiched droplet appears to determine the properties of the 2D Au NP array, such as the density of Au NPs, aggregation, and stacking. In subsequent

studies, the sandwiched droplet was dried in a thermo-hygrostat bath to stabilize and control the evaporation rate.

Optimization of the Drying Conditions during the SW Technique. To analyze the effect of the evaporation rate on the formation of the 2D Au NP array, we prepared Au NP arrays using the SW technique at different temperatures and humidities. First, we examined the effect of temperature on the formation of 2D Au NP arrays. Figure S1a–c show SEM images ($\times 10,000$) of 2D Au NP arrays formed at a relative humidity of $60 \pm 10\%$ and temperatures of 293, 298, and 303 K, respectively. These SEM images reveal magnified views of the outermost steps of the step-by-step structures. Figure S1a shows a 2D Au NP array formed at a relatively low temperature, with large voids and several Au NP aggregates observed. Moreover, the Au NPs appear to be stacked on the left of the black centerline. Figure S1c shows a 2D Au NP array formed at a relatively high temperature, with numerous large Au NP aggregates observed.

Conversely, in Figure S1b, the 2D Au NP arrays appear to be monolayer, with almost no aggregation. Subsequently, humidity conditions were examined. Two 2D Au NP arrays prepared using the SW technique at 298 K with relative humidity of $60 \pm 10\%$ (SW-substrate 1) and $20 \pm 5\%$ (SW-substrate 2) were observed. Figure 2b shows an SEM image ($\times 20,000$) of SW-substrate 1, with the Au NPs observed in a dense 2D arrangement. Figure 2c shows an SEM image ($\times 20,000$) of SW-substrate 2. At this humidity, the evaporation rate is double that observed at a relative humidity of 60%. Numerous small islands consisting of several Au NPs are observed, and the distances between each island are several tens of nanometers. The density of Au NPs in SW-substrate 2 is lower than that in SW-substrate 1. Therefore, the optimal temperature and relative humidity are 298 K and $60 \pm 10\%$, respectively. Moreover, the quality of the 2D Au NP array is highly and sensitively dependent on the drying temperature and humidity.

For comparison, two substrates were also prepared using the OW and DD methods. Figure 3a shows an SEM image ($\times 2000$) of the OW-substrate, with several defects and 3D aggregates observed. Figure 3b shows an SEM image ($\times 20,000$) of the DD-substrate, with isolated Au NPs and several Au NP aggregates scattered randomly.

Characterizations of 2D Au NP Arrays. The obtained SEM images were divided into 500×500 nm regions to evaluate the densities and uniformities of the 2D Au NP arrays. The packing densities in each region were determined using the areas of the Au NPs. Table 1 summarizes the packing densities and their relative standard deviations (RSDs, $n = 96$). The packing densities of the Au NPs are ordered as follows: SW-substrate 1 (78%) > SW-substrate 2 (73%) > OW-substrate (65%) > DD-substrate (16%). Their RSDs are ordered as follows: SW-substrate 1 (3.1%) < SW-substrate 2 (5.5%) < OW-substrate (6.1%) < DD-substrate (71%). Compared to those of OW and DD substrates, the SW substrates exhibit high Au NP densities and uniformities. Additionally, SW-substrate 1 exhibits a higher density and uniformity than those of SW-substrate 2 due to the effect of humidity on the evaporation rate of the Au NP colloidal solution.

A highly uniform particle array likely exhibits a periodic array structure, and Fourier transform (FT) analyses were performed on SEM images to evaluate the periodicities of the arrangements. Figure 2b,c show the FTs of the SEM data of SW-substrates 1 and 2, respectively. Bright spots are observed in these two images at the vertices of hexagons. Therefore, SW-substrates 1

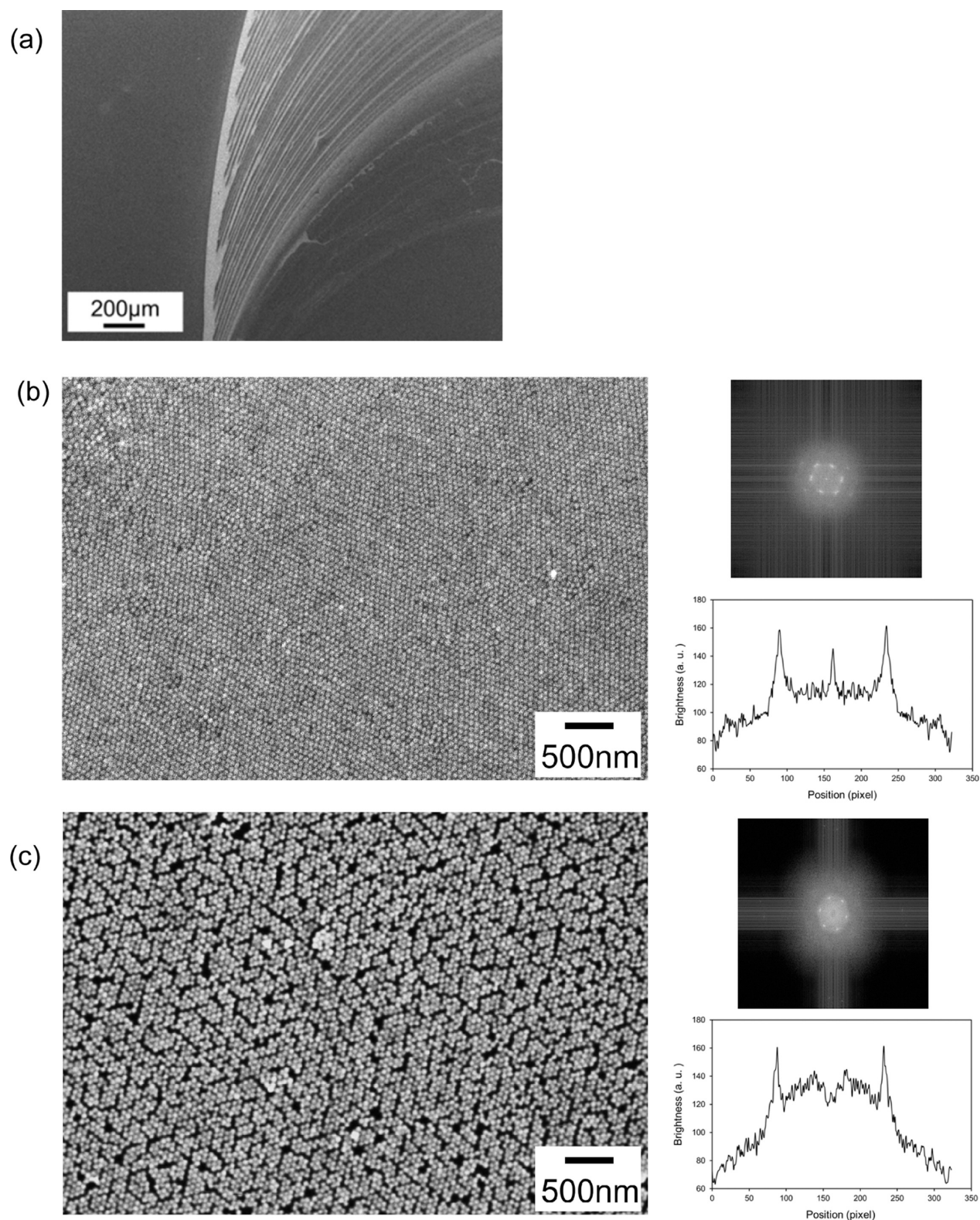


Figure 2. (a) SEM image at $\times 50$ magnification of SW-substrate 1 on the Si wafer, which was prepared at a relative humidity of $60 \pm 10\%$ at 298 K. (b) SEM image at $\times 20,000$ magnification of SW-substrate 1. (c) SEM image at $\times 20,000$ magnification of SW-substrate 2, which was prepared at a relative humidity of $20 \pm 5\%$ at 298 K. These substrates were composed of spherical Au NPs (mean diameter: 60 nm). Corresponding FFT images and their brightness distribution are shown in the higher right and lower right, respectively.

and 2 exhibit periodicities of six-fold symmetry. However, the packing density of 78% observed for SW-substrate 1 is smaller than that of 91% expected for an ideal 2D hexagonal close-packed structural configuration. The FT of SW-substrate 1 data

was then analyzed to explain this difference. The hexagonal lattice constant of SW-substrate 1 is 64.5 nm. Because the Au NPs exhibit an average diameter of 60 nm, this indicates that the Au NPs in SW-substrate 1 are not in contact with each other,

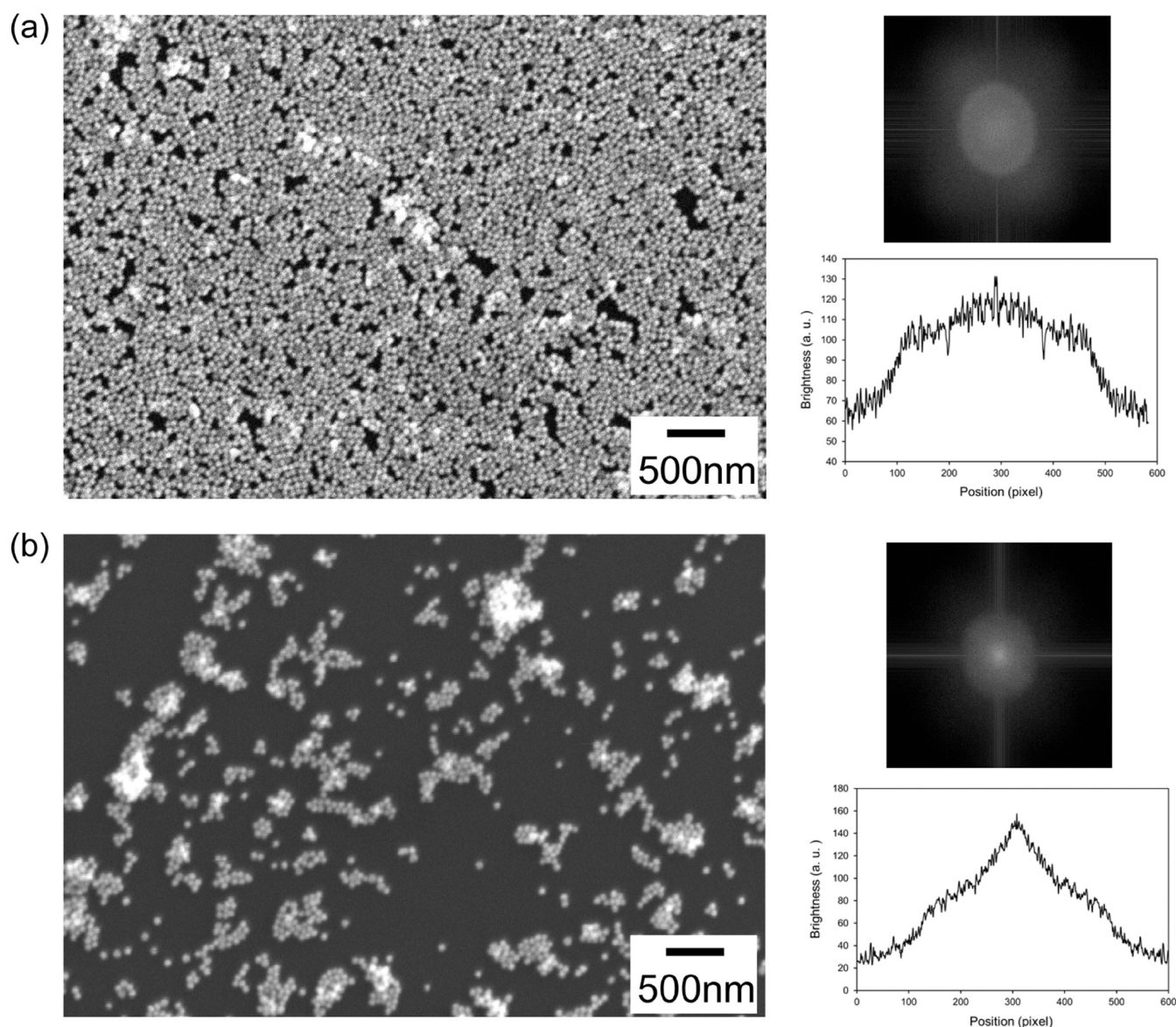


Figure 3. (a) SEM image at $\times 20,000$ magnification of the OW-substrate on the Si wafer. (b) SEM image at $\times 20,000$ magnification of the DD-substrate on Si wafer. These substrates were composed of spherical Au NPs (mean diameter: 60 nm). Corresponding FFT images and their brightness distribution are shown in the higher right and lower right, respectively.

Table 1. Packing Densities and Their RSDs of Four Substrates

substrate	packing density (%)	RSD (%)
SW-substrate 1	78	3.1
SW-substrate 2	73	5.5
OW-substrate	65	6.1
DD-substrate	16	71

with an average interparticle distance of ~ 4.5 nm. When the interparticle distance is 4.5 nm, the ideal packing density of a 2D hexagonal-packed configuration is 81%. The 3% difference in the recalculated (81%) and experimental (78%) packing densities of SW-substrate 1 may be attributed to minor defects. Conversely, as shown in Figure 3a,b, no such bright spots are observed in the FT images of the other substrates. These Au NP assemblies in the OW and DD substrates exhibit no periodicities.

Figure 4 shows the vis–NIR extinction spectra of SW-substrate 1 (black line), the OW and DD substrates (green and

red lines, respectively), and Au NP colloidal solution (dotted line). The spectrum of SW-substrate 1 exhibits two peaks at 547 and 750 nm. The spectrum of the OW substrate exhibits a broad peak in the region 600–1000 nm, whereas that of the DD substrate exhibits a single peak at 540 nm. The spectrum of the Au NP colloidal solution exhibits a single peak at 537 nm, corresponding to the LSPR of isolated spherical Au NPs in water. The peaks at 547 and 540 nm in the spectra of SW-substrate 1 and the DD substrate, respectively, may be attributed to the red-shifted LSPR peak representing isolated spherical Au NPs. Therefore, either most Au NPs in SW-substrate 1 and the DD substrate are isolated from their neighbors or the numbers and sizes of the aggregated Au NPs are small. This is consistent with the SEM observations and the FT analyses. The red-shift distance from the isolated spherical Au NP LSPR peak to that observed for SW-substrate 1 is 10 nm, whereas the shift distance to that observed for the DD substrate is 3 nm. The LSPR peak wavelength depends on the plasmonic coupling of neighboring Au NPs. Therefore, the large red-shift observed for SW-substrate

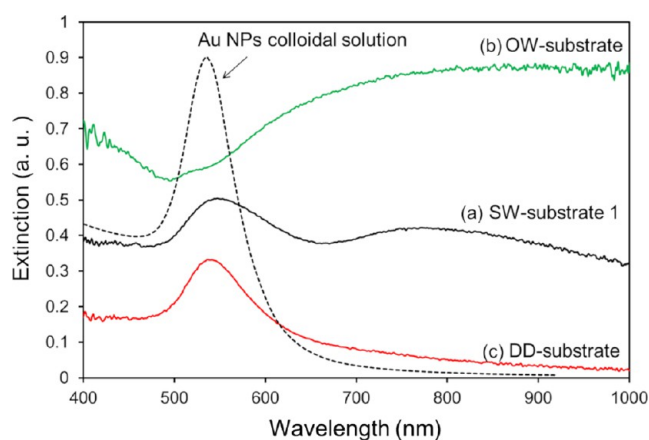


Figure 4. Vis–NIR Extinction spectra of (a) SW-substrate 1, (b) OW-substrate, and (c) DD-substrate. These substrates were on glass slides. The dotted line indicates vis–NIR absorption spectra of spherical Au NP (mean diameter: 60 nm) colloidal solution, which was used for the preparation of these substrates.

1 is due to plasmonic coupling. For SW-substrate 1, a peak at 750 nm is also observed. When several Au NPs are close, with interparticle distances of several nanometers, an additional peak is observed at a longer wavelength in the vis–NIR extinction spectrum. Hentschel et al. showed that the extinction spectra of Au NP heptamers with interparticle gaps exhibited new extinction peaks in the NIR region when the gap distance was <60 nm.²⁷ They concluded that this additional extinction peak was caused by a plasmonic oligomer transition from isolated to collective modes. Although there are several differences between the experimental conditions in this study and those of other groups, the previously reported extinction spectra are similar to those of SW-substrate 1. Therefore, the peak in the spectrum of SW-substrate 1 at 750 nm is due to LSPR coupling. For the OW substrate, the LSPR peak representing the isolated Au NPs almost entirely disappears, with a broad peak emerging from 600 to 1000 nm. When Au NPs aggregate randomly, these aggregates exhibit broad, longer wavelength peaks due to their various plasmon modes. Therefore, the spectrum of the OW substrate indicates that almost all Au NPs are randomly aggregated.

SERS Properties of 2D Au NP Arrays. To investigate the SERS properties of SW-substrate 1, CV was used as a test molecule because it is well studied in SERS.^{28,29} Here, uniform adsorption of CV on the Au NP surfaces was required to evaluate the spot-to-spot reproducibility of SERS signals representing the nanostructures of the SERS substrates. CV molecules are chemically adsorbed on the surface of Au. Thus, by immersing the SERS substrate in the CV solution, the CV molecules may be chemically adsorbed on the surfaces of the Au NPs as a monolayer after washing and removing the physically adsorbed CV molecules. The immersion time was determined via SERS measurements using OW substrates (Figure S2), and the immersion time for saturation adsorption was set at 1000 s. Figure 5a shows the Raman spectrum of CV molecules chemically adsorbed on SW-substrate 1 at an excitation wavelength of 532 nm, and Table 2 shows the assignments of these peaks in previous studies.³⁰

No signals other than those derived from CV molecules were observed. This result suggests that no molecules other than sample CV molecules are adsorbed on the Au NPs' surface and that the Au NPs are bare, at least after substrate fabrication. In addition, we have previously reported that laser desorption/

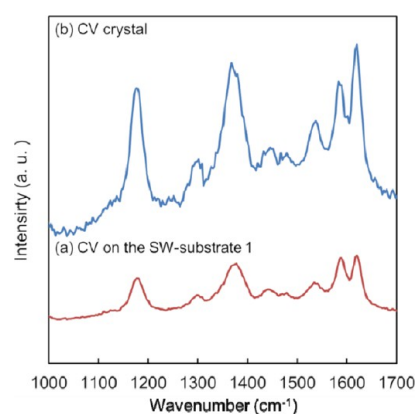


Figure 5. (a) Raman spectra of CV adsorbed on SW-substrate 1 and (b) Raman spectra of CV crystals. 532 nm lines of Nd:YAG laser was employed as the excitation laser.

Table 2. Assignment of Raman Bands of CV Crystal and CV Adsorbed on SW-Substrate 1

band (cm ⁻¹) crystal	band (cm ⁻¹) on SW substrate 1	assignment
1620	1621	C-phenyl in-plane antisymmetric stretching
1583	1584	C-phenyl in-plane antisymmetric stretching
1532	1537	phenyl-N antisymmetric stretching
1376	1380	C–N, phenyl-C-phenyl antisymmetric stretching
1175	1179	C-phenyl, C–H in-plane antisymmetric stretching

ionization mass spectrometry detects surface adsorbed species on the Au NPs with high sensitivity.³¹ Like the present study, when CV molecules were adsorbed on gold NPs, no signals other than CV molecules were observed in either the positive or negative ion mode. This report also supports that the Au NPs are bare after washing with water.

To estimate the SERS enhancement factor (EF) of SW-substrate 1, the number of CV molecules adsorbed on the Au NPs was calculated using the surface area, packing density, irradiation area of the laser, and adsorption area of CV. The most prominent peak at 1621 cm⁻¹ was used to perform the EF calculations. The laser irradiation area was 10 μm², and the CV molecules were approximated as circles with diameters of ~1 nm. Assuming that CV molecules were adsorbed to the upper half of an Au NP, 7200 CV molecules were adsorbed per Au NP. The number of CV molecules contributing to the Raman signal was 10⁷–10⁸ molecules per spot, or 1.7 × 10⁻¹⁶ mol. The typical Raman spectrum of the CV crystal (from 10¹² to 10¹³ molecules per spot) was also measured, as shown in Figure 5b. Therefore, the average EF of SW-substrate 1 was 10⁵–10⁶. The EFs were within the range of average reported values for Au NPs on a solid substrate (10⁴–10⁸).^{32,33} Furthermore, the OW and DD substrates exhibited sufficient SERS activities at certain points. However, the average EFs of these substrates were 1–2 orders of magnitude lower than that of SW-substrate 1.

The spot-to-spot reproducibility of SW-substrate 1 was then examined for three prominent bands at 1179, 1380, and 1621 cm⁻¹. Figure 6a–c show the normalized peak intensity of each CV band in the SERS spectra measured at 32 different points on the same substrate, and Figure 6d shows their RSDs. The packing density is used as a uniformity index to compare the

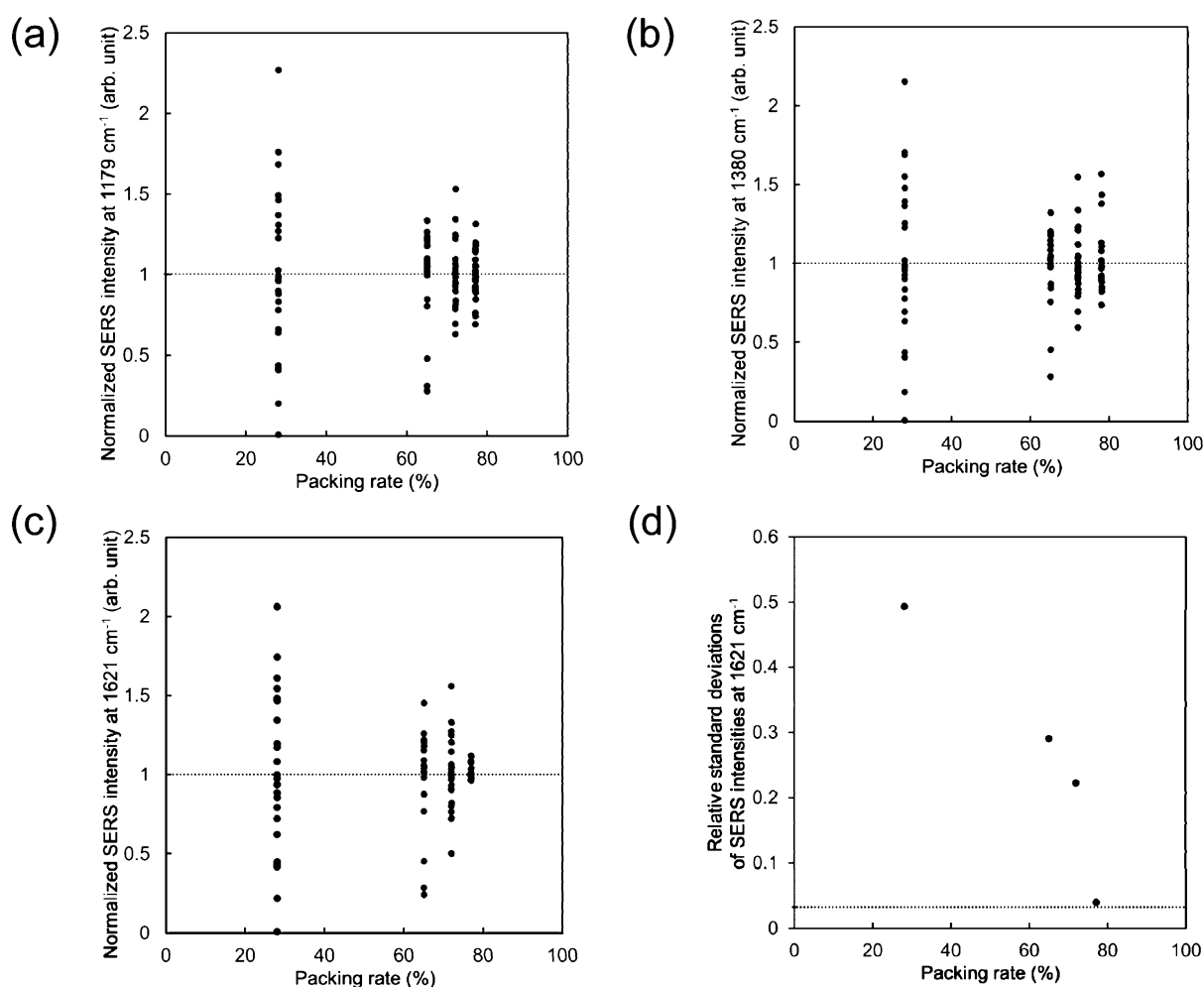


Figure 6. Normalized peak intensities of bands at (a) 1179 cm⁻¹, (b) 1380 cm⁻¹, and (c) 1621 cm⁻¹ versus packing rates of four substrates. The mean value was normalized to 1 (dotted line). These peak intensities were obtained from different 25 spots in these substrates. (d) RSDs of SERS intensities at 1621 cm⁻¹ versus packing rates of four substrates. The dotted line indicates the systematic error obtained from a silicon single crystal (100).

different substrates and is set as the horizontal axis. As the packing density increases, the variation in the peak intensity of each band decreases, and those observed for SW-substrate 1, with a packing density of 78%, exhibit the smallest value (3.1%). This RSD value is lower than previous SERS studies using Au NPs shown in Table S3, indicating very high spot-to-spot reproducibility, although simple comparisons are difficult due to the different experimental conditions. Surprisingly, the RSD of SW-substrate 1 is similar to that of a systematic error obtained by a spot-to-spot Raman measurement on a Si single crystal, as shown in Figure 6d. Therefore, a sufficiently uniform EM field is generated over the entire SW-substrate 1 for a spot area of $\sim 10 \mu\text{m}^2$. In addition, as the packing density increases, the RSD decreases significantly.

The improvement in reproducibility due to the increased packing ratio varies according to the band. The improvement in reproducibility of the band at 1621 cm⁻¹ is particularly remarkable. Although the cause of this remains unclear, these differences are likely caused by the adsorption states of the CV molecules and their associated charge transfer (CT) enhancement,³⁴ which is observed for molecules chemisorbed on a bare metal surface. According to previous reports,^{35,36} these factors exhibit different effects on each vibration band associated with chemisorption. As shown in Table 2, shifts due to chemisorption are observed in several vibration bands, with varying degrees of

shifting. However, the band at 1621 cm⁻¹ is not significantly shifted. Thus, the effects of CV molecule adsorption and CT enhancement on the band at 1621 cm⁻¹ are relatively small. The EM enhancement may be relatively high for the 1621 cm⁻¹ band, and the high uniformity of SW-substrate 1 directly reflects the reproducibility. A more detailed study should be conducted to study the contribution of CT enhancement to the reproducibility of SERS measurements.

Mechanistic Considerations of the SW Technique. A series of studies revealed that SW-substrate 1 exhibits a uniform arrangement without Au NP aggregation, although organic surface-modifying molecules are not used to modify the Au NP surfaces. Furthermore, the high spot-to-spot reproducibility of the SERS measurements supports the high uniformity of the nanostructure of SW-substrate 1. We investigated the formation of this array by observing the formation of the 2D Au NP array and the final array structure using an optical microscope.

In the early stage of evaporation at $t = 45$ min, the Au NPs are concentrated on the contact line, as shown in Figure 1a. In general, the solute reaches equilibrium at a uniform concentration via diffusion within the solution. Therefore, this non-equilibrium state is due to a mechanism, such as convection, which supplies Au NPs to the edge of the contact line. In addition, as shown in Figure 1a, the contact angle is 0° at the edge of the contact line. This sharp contact line hinders the

formation of 3D aggregates because the height of the droplet at the edge is insufficient for supplying Au NPs to the second layer at the edge of the contact line. No stacking is observed under the optimized drying conditions.

Au NPs concentrated at the edge of the contact line remain dispersed in the liquid before forming the 2D Au NP array, as shown in Figure 1c. According to calculations based on DLVO theory, the potential barriers of Au NPs dispersed in water are located at an interparticle distance of several nanometers, and they aggregate when they are closer than the potential barrier. Because no aggregation is observed in SW-substrate 1, the Au NPs may maintain a state wherein the repulsion between the particles dominates until the 2D Au NP array is formed, with the kinetic energy not exceeding the potential barrier. On the other hand, formation of numerous aggregates when the SW technique is performed at 303 K, a relatively high temperature, as shown in Figure S1. We considered that the kinetic energy exceeds the potential barrier at this temperature, thus causing aggregation.

Smooth movement of the contact line is observed with the formation of the 2D Au NP array, as shown in Figure 1b. Generally, the contact line of a simple droplet on a flat plate is pinned, maintaining its initial position when the solvent dries. In this case, the solute concentrates at the contact line, forming a ring, denoted the coffee-ring effect.³⁷ This causes a concentration of the solute at the edges of the droplet, leading to aggregation. However, during the SW technique, the pinning of the contact line is suppressed. The movement of the contact line is more likely to occur than the shape variation of the meniscus that is stabilized in the capillary bridge. This movement of the contact line prevents a supply of excess Au NPs to the contact line and suppresses the aggregation of the Au NPs.

In summary, we considered three factors contributing to the formation of a uniform 2D Au NP array using the SW technique. First, Au NPs were supplied to the edge of the sharp contact line. Second, the Au NPs were gently concentrated without energy addition. Third, the half-moon meniscus moved as the droplet dried, without pinning the contact line. These factors depended on the drying conditions, such as the temperature and humidity. Under suitable drying conditions, the Au NPs were concentrated at the edge of the contact line while maintaining the repulsion between particles. As a result, the Au NP arrangement was highly ordered, without aggregation, and without an organic surface modifier. The step-by-step structures observed in Figures 1b and 2a were formed due to the balance between the supply rate of Au NPs to the edge of the contact line and the rate of motion of the contact line.

CONCLUSIONS

We investigated the SW technique to form uniform 2D bare Au NP arrays using colloidal dispersions of Au NPs. First, the formation of the 2D Au NP arrays using the SW technique was observed using an optical microscope to determine the effective synthetic parameters of a uniform 2D bare Au NP array. The supply of Au NPs to the edge of the contact line and the formation of the Au NP assembly were observed as the droplets dried. Based on these observations, we focused on and optimized the drying conditions. The most uniform 2D Au NP array was formed at 298 K and a relative humidity of 60%. SW-substrate 1 formed under the optimized conditions exhibited a hexagonal closely packed structure with an average interparticle distance of 4.5 nm without aggregation. Although the ideal densest packing ratio in this case was 81%, the packing

ratio of SW-substrate 1 was 78%, indicating a very high packing ratio. In the extinction spectrum of SW-substrate 1, peaks due to the LSPR of the Au NPs and plasmon coupling were observed. Compared to those of conventional 2D Au NP arrays, such as the DD and OW substrates, the uniformity of the SW substrate was extremely high. Furthermore, the SW substrate showed excellent SERS enhancement, with an RSD of 3.1% for its signal intensity, which is comparable to the systematic error of the present Raman measurements, indicating a very high spot-to-spot reproducibility. To the best of our knowledge, the SW technique is the simplest method that enables the formation of a uniform 2D bare Au NP array with interparticle gaps. In the future, it may be possible to control the interparticle gap by controlling the repulsion between the NPs. Thus, use of the SW technique may lead to the development of molecular sensors and plasmonics.

ASSOCIATED CONTENT

Supporting Information

The Supporting Information is available free of charge at <https://pubs.acs.org/doi/10.1021/acsomega.2c04032>.

SEM images of SW substrates, dependence of Raman peak intensity on the dipping time, and literature data for SERS substrates using Au NPs (DOCX)

AUTHOR INFORMATION

Corresponding Author

Kohei Shibamoto – Department of Chemistry, Graduate School of Science, Tokyo Metropolitan University, Hachioji, Tokyo 192-0397, Japan; orcid.org/0000-0003-2559-6739; Phone: +81-42-677-2531; Email: shiba@tmu.ac.jp

Author

Takashi Fujita – Department of Applied Chemistry, School of Engineering, Tokyo University of Technology, Hachioji, Tokyo 192-0982, Japan

Complete contact information is available at: <https://pubs.acs.org/10.1021/acsomega.2c04032>

Author Contributions

The manuscript was written through contributions of all authors. All authors have given their approval to the final version of the manuscript.

Notes

The authors declare no competing financial interest.

ACKNOWLEDGMENTS

This work was supported by JSPS KAKENHI grant no. JP18K04730 (K.S.) and JSPS KAKENHI grant no. JP19K15410 (T.F.).

ABBREVIATIONS

CT	charge transfer
CV	crystal violet
DD	dried droplet
DLVO	Derjaguin–Landau–Verwey–Overbeek
EF	enhancement factor
EM	electromagnetic
FT	Fourier transform
LSPR	localized surface plasmon resonance
NP	nanoparticle
OW	oil–water trapping

RSD, relative standard deviation;
SEM scanning electron microscopy
SERS surface-enhanced Raman scattering
SW sandwich
vis-NIR visible-near-infrared

REFERENCES

- (1) Mayer, K. M.; Hafner, J. H. Localized Surface Plasmon Resonance Sensors. *Chem. Rev.* **2011**, *111*, 3828–3857.
- (2) Jiang, N.; Zhuo, X.; Wang, J. Active Plasmonics: Principles, Structures, and Applications. *Chem. Rev.* **2018**, *118*, 3054–3099.
- (3) Kleinman, S. L.; Frontiera, R. R.; Henry, A. I.; Dieringer, J. A.; Van Duyne, R. P. Creating, Characterizing, and Controlling Chemistry with SERS Hot Spots. *Phys. Chem. Chem. Phys.* **2013**, *15*, 21–36.
- (4) Sharma, B.; Frontiera, R. R.; Henry, A. I.; Ringe, E.; Van Duyne, R. P. SERS: Materials, Applications, and the Future. *Mater. Today* **2012**, *15*, 16–25.
- (5) Huang, Z.; Zhang, A.; Zhang, Q.; Cui, D.; Nanomaterial-Based, S. E. R. S. Nanomaterial-Based SERS Sensing Technology for Biomedical Application. *J. Mater. Chem. B* **2019**, *7*, 3755–3774.
- (6) Sackmann, M.; Materny, A. Surface Enhanced Raman Scattering (SERS) – A Quantitative Analytical Tool? *J. Raman Spectrosc.* **2006**, *37*, 305–310.
- (7) De Rosa, C.; Auriemma, F.; Diletto, C.; Di Girolamo, R.; Malafrente, A.; Morvillo, P.; Zito, T.; Rusciano, G.; Pesce, G.; Sasso, A. Toward hyperuniform disordered plasmonic nanostructures for reproducible surface-enhanced Raman spectroscopy. *Phys. Chem. Chem. Phys.* **2015**, *17*, 8061–8069.
- (8) Le Ru, E. C.; Etchegoin, P. G.; Grand, J.; Félidj, N.; Aubard, J.; Lévi, G.; Hohenau, A.; Krenn, J. R. Surface Enhanced Raman Spectroscopy on Nanolithography-Prepared Substrates. *Curr. Appl. Phys.* **2008**, *8*, 467–470.
- (9) Das, G.; Mecarini, F.; Gentile, F.; De Angelis, F.; Mohan Kumar, M.; Candeloro, P.; Liberale, C.; Cuda, G.; Di Fabrizio, E. Nano-patterned SERS substrate: Application for protein analysis vs. temperature. *Biosens. Bioelectron.* **2009**, *24*, 1693–1699.
- (10) Reincke, F.; Hickey, S. G.; Kegel, W. K.; Vanmaekelbergh, D. Spontaneous Assembly of a Monolayer of Charged Gold Nanocrystals at the Water/Oil Interface. *Angew. Chem., Int. Ed. Engl.* **2004**, *43*, 458–462.
- (11) Pienpinijtham, P.; Han, X. X.; Ekgasit, S.; Ozaki, Y. An Ionic Surfactant-Mediated Langmuir – Blodgett Method to Construct Gold Nanoparticle Films for Surface-Enhanced Raman Scattering. *Phys. Chem. Chem. Phys.* **2012**, *14*, 10132–10139.
- (12) Guo, Q.; Xu, M.; Yuan, Y.; Gu, R.; Yao, J. Self-Assembled Large-Scale Monolayer of Au Nanoparticles at the Air/Water Interface Used as a SERS Substrate. *Langmuir* **2016**, *32*, 4530–4537.
- (13) Liu, D.; Li, C.; Zhou, F.; Zhang, T.; Liu, G.; Cai, W.; Li, Y. Capillary Gradient-Induced Self-Assembly of Periodic Au Spherical Nanoparticle Arrays on an Ultralarge Scale via a Bisolvent System at Air/Water Interface. *Adv. Mater. Interfaces* **2017**, *4*, 1600976.
- (14) Liu, S.; Zhu, T.; Hu, R.; Liu, Z. Evaporation-Induced Self-Assembly of Gold Nanoparticles into a Highly Organized Two-Dimensional Array. *Phys. Chem. Chem. Phys.* **2002**, *4*, 6059–6062.
- (15) Yang, G.; Nanda, J.; Wang, B.; Chen, G.; Hallinan, D. T., Jr. Self-Assembly of Large Gold nanoparticles for Surface-Enhanced Raman Spectroscopy. *ACS Appl. Mater. Interfaces* **2017**, *9*, 13457–13470.
- (16) Israelachvili, J. N.; *Intermolecular and Surface Forces*, 3rd ed.; Academic Press, 2011.
- (17) Njoki, P. N.; Lim, I. S.; Mott, D.; Park, H.; Khan, B.; Mishra, S.; Sujakumar, R.; Luo, J.; Zhong, C. Size Correlation of Optical and Spectroscopic Properties for Gold Nanoparticles. *J. Phys. Chem. C* **2007**, *111*, 14664–14669.
- (18) Zhang, P.; Li, Y.; Wang, D.; Xia, H. High-Yield Production of Uniform Gold Nanoparticles with Sizes from 31 to 577 nm via One-Pot Seeded Growth and Size-Dependent SERS Property. *Part. Part. Syst. Charact.* **2016**, *33*, 924–932.
- (19) Park, Y. K.; Yoo, S. H.; Park, S. Assembly of Highly Ordered Nanoparticle Monolayers at a Water/Hexane Interface. *Langmuir* **2007**, *23*, 10505–10510.
- (20) Kim, B.; Tripp, S. L.; Wei, A. Self-Organization of Large Gold Nanoparticle Arrays. *J. Am. Chem. Soc.* **2001**, *123*, 7955–7956.
- (21) Ishida, T.; Tachikiri, Y.; Sako, T.; Takahashi, Y.; Yamada, S. Structural Characterization and Plasmonic Properties of Two-Dimensional Arrays of Hydrophobic Large Gold Nanoparticles Fabricated by Langmuir-Blodgett Technique. *Appl. Surf. Sci.* **2017**, *404*, 350–356.
- (22) Wang, H.; Levin, C. S.; Halas, N. J. Nanosphere Arrays with Controlled Sub-10-Nm Gaps as Surface-Enhanced Raman Spectroscopy Substrates. *J. Am. Chem. Soc.* **2005**, *127*, 14992–14993.
- (23) Wei, A.; Kim, B.; Pusztay, S. V.; Tripp, S. L.; Balasubramanian, R. Resorcinarene-Encapsulated Nanoparticles Building Blocks Self-Assembled Nanostructures. *J. Inclusion Phenom.* **2001**, *41*. DOI: [10.1023/A:1014472212238](https://doi.org/10.1023/A:1014472212238)
- (24) Smith, S. R.; Lipkowski, J. Guided Assembly of Two-Dimensional Arrays of Gold Nanoparticles on a Polycrystalline Gold Electrode for Electrochemical Surface-Enhanced Raman Spectroscopy. *J. Phys. Chem. C* **2018**, *122*, 7303–7311.
- (25) Shibamoto, K.; Yasumuro, S.; Horiuchi, K.; Teraoka, T.; Fujita, T. Study of Two-dimensional Highly-ordering of Gold Nanoparticles for an Optical Sensor Using Surface Plasmon Excitation as an Assistance Effect. *Bunseki Kagaku* **2014**, *63*, 293–298.
- (26) Shibamoto, K.; Kitajima, M.; Mohammad, K. H.; Patent, K. I. Fabrication of single layer array structure of surface unmodified metal nanoparticles. JP 4900550 B2, 2012.
- (27) Hentschel, M.; Dregely, D.; Vogelgesang, R.; Giessen, H.; Liu, N. Plasmonic Oligomers: The Role of Individual Particles in Collective Behavior. *ACS Nano* **2011**, *5*, 2042–2050.
- (28) Kneipp, K.; Kneipp, H.; Itzkan, I.; Dasari, R. R.; Feld, M. S. Single Molecule Detection Using near Infrared Surface-Enhanced Raman Scattering. *Single Molecule Spectroscopy*; Series in Chemical Physics; Springer, 2001; pp 144–160.
- (29) Jiang, J. D.; Burstein, E.; Kobayashi, H. Resonant Raman Scattering by Crystal-Violet Molecules Adsorbed on a Smooth Gold Surface: Evidence for a Charge-Transfer Excitation. *Phys. Rev. Lett.* **1986**, *57*, 1793–1796.
- (30) Cañamares, M. V.; Chenal, C.; Birke, R. L.; Lombardi, J. R. DFT, SERS, and Single-Molecule SERS of Crystal Violet. *J. Phys. Chem. C* **2008**, *112*, 20295–20300.
- (31) Shibamoto, K.; Sakata, K.; Nagoshi, K.; Korenaga, T. Laser Desorption Ionization Mass Spectrometry by Using Surface Plasmon Excitation on Gold Nanoparticle. *J. Phys. Chem. C* **2009**, *113*, 17774–17779.
- (32) Vinod, M.; Gopchandran, K. G. Au, Ag and Au:Ag Colloidal Nanoparticles Synthesized by Pulsed Laser Ablation as SERS Substrates. *Prog. Nat. Sci.: Mater. Int.* **2014**, *24*, 569–578.
- (33) Lin, S.; Lin, X.; Song, X.; Han, S.; Wang, L.; Hasi, W. Fabrication of Flexible Paper - Based Surface - Enhanced Raman Scattering Substrate from Au Nanocubes Monolayer for Trace Detection of Crystal Violet on Shell. *J. Raman Spectrosc.* **2019**, *50*, 1074–1084.
- (34) Kneipp, K.; Kneipp, H.; Itzkan, I.; Dasari, R. R.; Feld, M. S. Ultrasensitive Chemical Analysis by Raman Spectroscopy. *Chem. Rev.* **1999**, *99*, 2957–2976.
- (35) Shibamoto, K.; Katayama, K.; Sawada, T. Fundamental Processes of Surface Enhanced Raman Scattering Detected by Transient Reflecting Grating Spectroscopy. *J. Photochem. Photobiol., A* **2003**, *158*, 105–110.
- (36) Shibamoto, K.; Katayama, K.; Sawada, T. Ultrafast Charge Transfer in Surface-Enhanced Raman Scattering (SERS) Processes Using Transient Reflecting Grating (TRG) Spectroscopy. *Chem. Phys. Lett.* **2007**, *433*, 385–389.
- (37) Deegan, R. D.; Bakajin, O.; Dupont, T. F.; Huber, G.; Nagel, S. R.; Witten, T. A. Capillary Flow as the Cause of Ring Stains from Dried Liquid Drops. *Nature* **1997**, *389*, 827–829.